ACS Photonics

Article

Cite This: ACS Photonics 2018, 5, 3372−3378

pubs.acs.org/journal/apchd5

Understanding the Image Contrast of Material Boundaries in IR Nanoscopy Reaching 5 nm Spatial Resolution

Stefan Mastel,[†] Alexander A. Govyadinov,[†] Curdin Maissen,[†] Andrey Chuvilin,[†,‡] Andreas Berger,[†] and Rainer Hillenbrand*[,‡,§]

[†]CIC nanoGUNE, 20018 Donostia-San Sebastián, Spain

[‡]IKERBASQUE, Basque Foundation for Science, 48013 Bilbao, Spain

[§]CIC nanoGUNE and UPV/EHU, 20018 Donostia-San Sebastián, Spain

Supporting Information

ABSTRACT: Scattering-type scanning near-field optical microscopy (s-SNOM) allows for nanoscale-resolved Infrared (IR) and Terahertz (THz) imaging, and thus has manifold applications ranging from materials to biosciences. However, a quantitatively accurate understanding of image contrast formation at materials boundaries, and thus spatial resolution is a surprisingly unexplored terrain. Here we introduce the read/write head of a commercial hard disk drive (HDD) as a most suitable test sample for fundamental studies, given its well-defined sharp material boundaries perpendicular to its ultrasmooth surface. We obtain unprecedented and unexpected insights into the s-SNOM image formation process, free of topography-induced contrasts that often mask and artificially modify the pure near-field optical contrast. Across metal-dielectric boundaries, we observe non-point-symmetric line profiles for both IR and THz illumination, which are fully corroborated by numerical simulations. We explain our findings by a sample-dependent confinement and screening of the near fields at the tip apex, which will be of crucial importance for an accurate understanding and proper interpretation of high-resolution s-SNOM images of nanocomposite materials. We also demonstrate that with ultrasharp tungsten tips the apparent width (resolution) of sharp material boundaries can be reduced to about 5 nm.

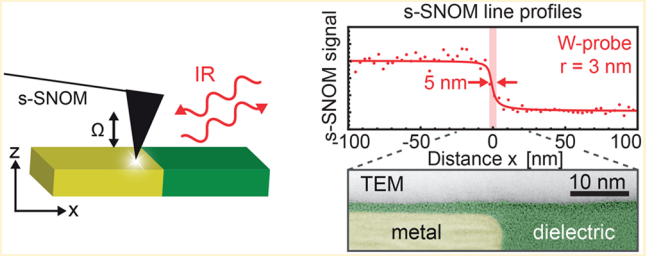

KEYWORDS: *scattering-type scanning near-field optical microscopy (s-SNOM), IR and THz nanoscopy, focused ion beam (FIB) machining, ultrasharp near-field probes*

Scattering-type Scanning near-Field Optical Microscopy (s-SNOM)[1] is a scanning probe technique for visible, infrared, and terahertz imaging and spectroscopy with nanoscale spatial resolution. It has proven large application potential ranging from materials characterization[2,3] to biosciences.[4,5] In s-SNOM, a metalized Atomic Force Microscope (AFM) tip is illuminated with p-polarized light. The tip acts as an antenna and concentrates the illumination at its apex to a near-field spot on the scale of the apex radius. When brought into close proximity to a sample, the near fields interact with the sample and modify the tip-scattered field.[6] By recording the tip-scattered field while scanning the sample, a near-field image is obtained. It is generally accepted that essentially the tip's apex radius determines the achievable resolution, which is typically in the range of a few tens of nanometers.[7,8] Although the resolution is a key parameter in s-SNOM, as in any other microscopy technique, it has been barely studied in detail experimentally.

The spatial resolution in microscopy is often evaluated by measuring the width of a typically point-symmetric line profile across the sharp boundary between two different materials.[9−11] Such a line profile can be considered as the so-called Edge Response Function (ERF). The characteristic width w of the ERF can be determined via its derivative, which is also known as the Line Spread Function (LSF). The LSF represents the image of a line-like object and is typically a bell-shaped symmetric function centered at the material boundary. The width of the LSF determines the resolution according to a specific criterion (e.g. Rayleigh or Sparrow).[12]

In s-SNOM experiments, w (often interpreted as the spatial resolution in analogy to other microscopy techniques) is typically measured directly in a line profile recorded across a boundary[13−16] or via its derivative.[17] Values as small as w = 10 to 40 nm (evaluated using different criteria) have been reported for a broad spectral range extending from visible to terahertz frequencies.[13,14,18] However, the boundary between two different materials typically exhibits a step in topography, which challenges the reliable evaluation of w due to tip−sample convolution,[19−22] potentially resulting in a large over- or underestimation. To tackle this problem, a sample with a

Received: May 14, 2018
Published: July 11, 2018

DOI: 10.1021/acsphotonics.8b00636
ACS Photonics 2018, 5, 3372−3378

well-defined sharp material boundary but without topographic features is highly desired.[19,20]

Here we introduce the read/write head of a Hard Disk Drive (HDD) as a truly topography-free resolution test sample, exhibiting nanoscale-defined metal-dielectric boundaries perpendicular to its ultrasmooth surface. It serves as an analogue to the knife-edge test target[10,11] in classical optical microscopy and allows for detailed analysis of the s-SNOM image contrast with metal tips of apex radii down to 3 nm. We demonstrate that with these tips the ERF width w (evaluated as full width half-maximum of the corresponding LSF) can be smaller than 5 nm. We further find, surprisingly, that the ERF in s-SNOM is not point-symmetric, yielding an asymmetric LSF. Its width depends on the side of the material boundary where it is evaluated. On the metal side, we find an unexpectedly short near-field probing range that can be 1 order of magnitude below the tip apex diameter, which we explain by screening of the tip's near field by the metal sample. We corroborate our results by numerical simulations and discuss the implications of our findings for the interpretation of s-SNOM images in general.

Figure 1 shows the experimental setup and the HDD read/write-head sample. For our experiments, we utilized a commercial s-SNOM (Neaspec GmbH). The tip was illuminated by either a CO_2 (λ_1 = 9.3 μm) or a THz (λ_2 = 158 μm) laser beam with the polarization plane parallel to the tips axis. The tip acts as an antenna and concentrates the incoming radiation at the tip apex. In close proximity to a sample, the near fields interact with the sample and modify the tip-scattered field. The tip-scattered light is recorded by the detector D1 (IR) or D2 (THz) and contains information about the local optical properties of the sample. An interferometric detection scheme, operated in synthetic optical holography (SOH) mode,[23] enables the recording of both amplitude s and phase φ images. For background suppression, the tip is oscillated vertically at a frequency Ω and the tip-scattered signal is demodulated at higher harmonics n of the cantilever oscillation frequency Ω, yielding background-free near-field amplitude s_n and phase φ_n images.

For evaluating the resolution of the setup employing different tips, we use the read/write head of a commercial HDD as a resolution test sample and, more specifically, the edge of one of its magnetic shield structures. The lower left inset in Figure 1 shows a false color Scanning Transmission Electron Microscopy (STEM) image of a cross section of the sample. The contrast in the image lets us recognize sharply separated areas of metal (marked yellow) and dielectric material (marked green). According to the manufacturer of the HDD,[24] the metal is Permalloy (Fe/Ni 20/80), and the dielectric is Al_2O_3. Further, we observe in the STEM image a dielectric capping layer of around 1.5 nm covering the metal and, thus, also the material boundary. Most importantly for s-SNOM imaging, the STEM image shows that the sample surface is smoothed down to the sub-nm scale, even in the sample area where the material changes abruptly.

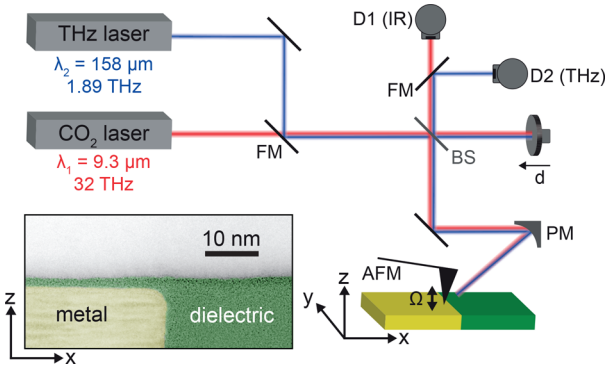

Figure 1. Schematics of the THz and IR s-SNOM setup. AFM, atomic force microscope; FM, flip mirror; BS, beam splitter; PM, parabolic mirror; D1, IR detector; D2, THz detector. The inset shows a STEM image of a cross section of our sample, which consists of the edge of a magnetic shield structure in a read/write head of a HDD.

Figure 2 shows the s-SNOM imaging results of the material boundary. As a near-field probe, we employed an 80 μm long Pt/Ir-tip (Rocky Mountain Nanotechnology, RM), operated at A = 25 nm tapping amplitude. We used long RM tips rather than standard cantilevered Pt/Ir-coated AFM tips (around 10 μm long) because of their better performance as near-field probes in the THz spectral range.[25,26] The RM tip radius of r = 23 nm is comparable to the standard metal-coated tips utilized in s-SNOM. We first recorded a topography image of the sample (Figure 2a), from which we extracted a line profile (Figure 2b) along the black dashed line. The line profile shows a maximum topography variation of 4 Å, which confirms the flatness of the sample. Simultaneously with topography, we recorded either IR (32 THz) and THz (1.89 THz) s-SNOM amplitude images s_2 to s_4. As an example, we show in Figure 2a the IR s_4 image. We observe two regions with high and low near-field amplitude signal, which lets us recognize the metal and dielectric material, respectively.[13,15]

To analyze the s-SNOM signal transition across the material boundary, we averaged 20 line profiles for each of the IR and THz images s_2 to s_4 (see Methods). The averaging ensures an accurate measurement of the apparent width of the material boundary, as individual line profiles can exhibit an untypically small or large width due to noise (see Supporting Information). The averaged line profiles (black dots) are shown in Figure 2c,d. In agreement with former observations, we observe that (i) the near-field contrast (i.e., the ratio between the near-field signal on metal and on dielectric material) increases for increasing demodulation orders n[27−29] and (ii) the contrast is higher for the IR than for THz. In order to better visualize the effect of the demodulation order on the near-field contrast, we show in the Supporting Information, S4, the same line profiles as in Figure 2c,d, but not vertically offset. The difference between the IR and THz material contrast can be attributed to frequency-dependent dielectric permittivities of the sample. Most important, and not having been recognized in previous s-SNOM experiments, the line profiles in Figure 2c,d are *not* point-symmetric, which we will study and discuss in the following.

The *asymmetric* line profiles require a careful analysis in order to properly interpret the s-SNOM contrast at material boundaries. As a first step toward this goal, we approximate the line profiles by the empirically found fit function:

$$\Theta(x) = \begin{cases} \pi^{-1} f_M \ \mathrm{Arctan}\left(\dfrac{x - x_0}{\gamma_M}\right) + b & \text{for } x < x_0 \\ \pi^{-1} f_D \ \mathrm{ArcTan}\left(\dfrac{x - x_0}{\gamma_D}\right) + b & \text{for } x \geq x_0 \end{cases}$$

DOI: 10.1021/acsphotonics.8b00636
ACS Photonics 2018, 5, 3372−3378

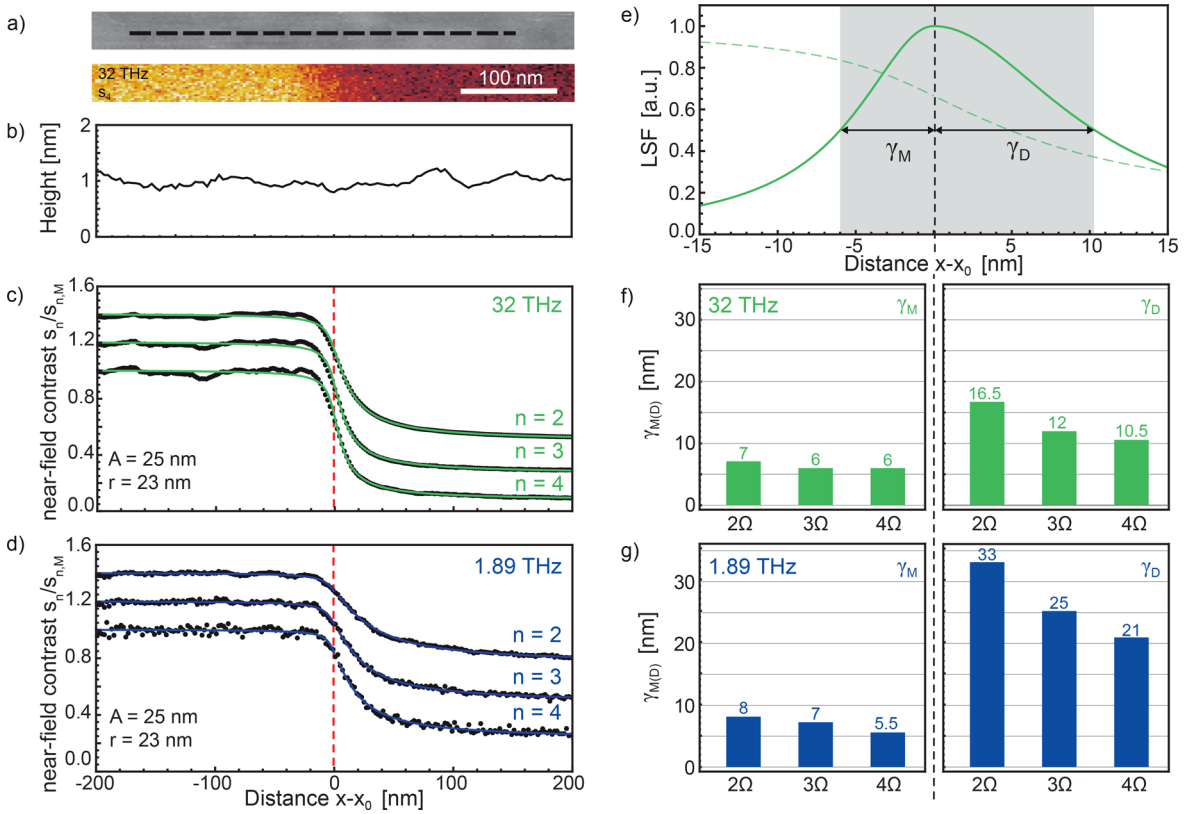

Figure 2. s-SNOM measurements on the resolution test sample. (a) AFM topography and IR s-SNOM amplitude s_4 (λ = 9.3 μm) images of sample. (b) Topography line profile extracted along the dashed line in (a). (c, d) Measured IR and THz near-field amplitude contrast $s_n/s_{n,M}$ line profiles (average of 20 line profiles, normalized to the amplitude signal on the metal, $s_{n,M}$) for harmonics n = 2 to 4 (black dots), and their respective fits using the integral of an asymmetric Lorentzian as described in text (green/blue lines). Tapping amplitude A = 25 nm, tip radius r = 23 nm. The curves are vertically offset for better visibility. (e) Derivative (solid line) of the fit of the s_4 line profile (dashed line) taken from (d). (f, g) HWHM $\gamma_{M(D)}$ of the derivatives of line profile fits in (c) and (d) on the metal and dielectric side, respectively.

with fit parameters x_0 (interface position) and b (vertical offset). To account for the asymmetry of the line profiles, the fit parameters $f_{M(D)}$ and $\gamma_{M(D)}$ assume different values for the metal ($x < x_0$) and the dielectric ($x \geq x_0$) sides. Further, the continuity of Θ and its derivative across the material interface is enforced. These fits are shown as green and blue solid curves in Figure 2c,d, excellently matching the experimental data. We note that the agreement between data and symmetric fits is much worse (see Supporting Information, S2), corroborating that indeed asymmetric fitting is required to correctly analyze the experimental line profiles. We next use these fits to quantify the asymmetry of the line profile. To that end, we calculate the derivative of the fit function $\Theta(x)$, which is given by a piecewise Lorentzian (exemplarily shown in Figure 2e for the IR s_4 line profile):

$$\mathcal{L}(x) = \begin{cases} \dfrac{f_M}{\pi} \dfrac{\gamma_M}{(x - x_0)^2 + \gamma_M^2} & \text{for } x < x_0 \\ \dfrac{f_D}{\pi} \dfrac{\gamma_D}{(x - x_0)^2 + \gamma_D^2} & \text{for } x \geq x_0 \end{cases}$$

with different half width at half maxima (HWHM) $\gamma_{M(D)}$ for the metal and the dielectric sides. Note that in the context of this work, we call this derivative the Line Spread Function (LSF) in analogy to the general concepts of resolution in classical optical microscopy, as described in the first section. The bar diagrams in Figures 2f,g summarize the different values for γ of the IR and THz measurements for demodulations orders n = 2 to 4. We find that the γ_D are about three to four times larger than the γ_M, quantifying the significant asymmetry of the line profiles. The total material boundary width w, defined as $w = \gamma_M + \gamma_D$, decreases from 23.5 to 16.5 nm (IR line profile) and from 41 to 26.5 nm (THz line profile) when the demodulation order increases from n = 2 to 4 (Figure 2f,g). The sharpening of the material boundary by higher-harmonic demodulation and the values for w agree well with previous studies[28,30,31] that, however, did not recognize the asymmetry of the profiles. Our quantitative analysis further shows that the material boundary is located not exactly central to the signal transition (see further discussion below), which is critical when a precise localization of a material boundary from s-SNOM profiles is desired. The analysis also shows that a significant near-field signal tail into one material does not necessarily indicate an unidirectional material gradient, for example, caused by unidirectional material diffusion. Our results clearly show that asymmetric line profiles with substantial levels of asymmetry can occur at well-defined sharp material boundaries, a fact that seems to be intrinsic to the near-field interaction and probing process. We will elucidate this phenomenon below.

To reduce the perceived width w of the material boundary in the s-SNOM line profile, that is, to increase the spatial resolution, we employed Focused Ion Beam (FIB) machining to fabricate Tungsten (W) tips with a reduced tip radius of only r = 3 nm (see upper right SEM image in Figure

DOI: 10.1021/acsphotonics.8b00636
ACS Photonics 2018, 5, 3372−3378

3).[8,25,32,33] Utilizing the ultrasharp full-metal W probes, we recorded line profiles across the material boundary at 32 THz

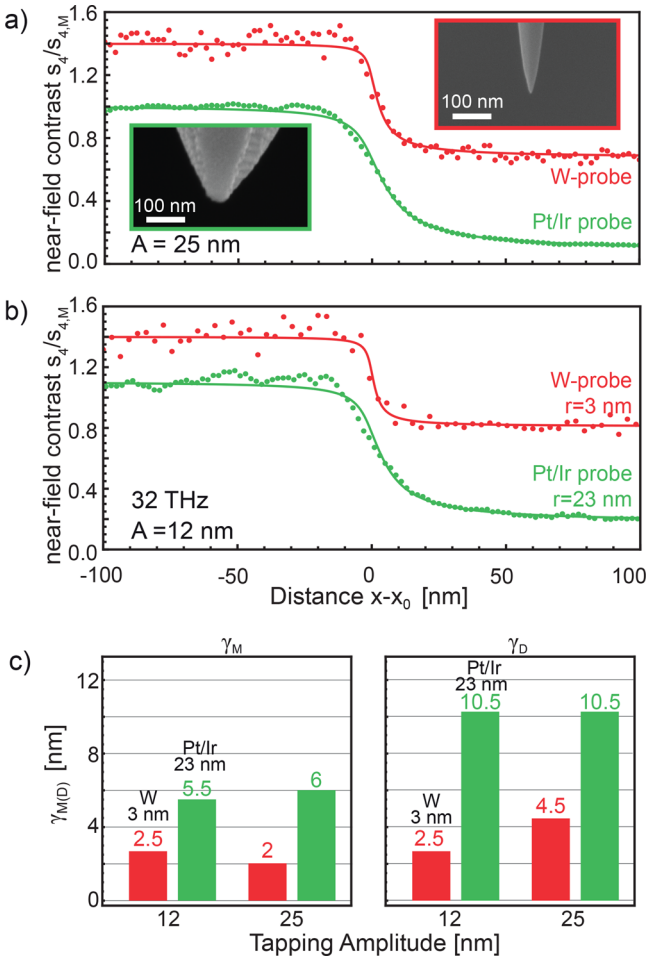

Figure 3. s-SNOM resolution test measurements for different probe sizes at 32 THz. (a) Near-field amplitude contrast $s_4/s_{4,M}$ line profiles recorded with ultrasharp W-tip (r = 3 nm; red dots) and commercial Pt/Ir-tip (r = 23 nm; green dots, same data as in Figure 2c) at A = 25 nm tapping amplitude. The green and red solid lines show the respective fits on the data. The upper right and lower left inset shows an SEM image of the W-tip and Pt/IR-tip, respectively. The curves are vertically offset for improved representation. (b) Near-field amplitude contrast $s_4/s_{4,M}$ line profiles and their respective fits recorded with ultrasharp W-tip (r = 3 nm; red) and commercial Pt/Ir-tip (r = 23 nm; green) at A = 12 nm tapping amplitude. (c) $\gamma_{M(D)}$ evaluated for the line profiles recorded with the W- and Pt/Ir-tips at A = 25 and 12 nm tapping amplitudes.

illumination and a tapping amplitude of A = 25 nm. The red dots in Figure 3a show the s_4 line profile (average of 50 profiles, see Methods) and the corresponding fit (red curve). For comparison we show the line profile obtained with the Pt/Ir probe (green; same data and fit as in Figure 2c). By measuring $\gamma_{M(D)}$ for both line profiles (summarized in Figure 3c), we find that w is reduced by more than a factor of 2 when the W-tip is used. The improvement, however, is surprisingly small, considering that the tip radius of the W-tip is around 8 times smaller than that of the Pt/Ir-tip. We attribute this finding to the relatively large tapping amplitude of A = 25 nm, which is comparable to the radius of the Pt/Ir-tip (r = 23 nm) but much larger than the radius of the W tip (r = 3 nm). According to previous studies,[28,34] the width w can be reduced by reducing the tapping amplitude. We thus recorded a line profile using both the Pt/Ir and W-tip with a reduced tapping amplitude of A = 12 nm (green and red data in Figure 3b, respectively). The resulting values for $\gamma_{M(D)}$ are shown in Figure 3c. For the Pt/Ir-tip, we measure w = 16.5 nm, which is comparable to that of the line profile at larger tapping amplitude A = 25. For the W-tip, the width w of the material boundary decreases further, to about 5 nm, which clearly demonstrates that ultrasharp metal tips can push the s-SNOM resolution well below 10 nm. We note that this reduction is mainly caused by the reduced γ_D of the LSF on the dielectric side of the material boundary. On the metal side, the 1.5 nm thick dielectric capping layer makes the metal/dielectric boundary a subsurface object (STEM image; Figure 1), for which the resolution is well-known to be diminished compared to objects directly at the surface.[28,35] It also has to be noted that numerous experiments reliably reveal a decrease of the s_n signal with decreasing tip diameter, which requires averaging of several line profiles to obtain sufficiently high signal-to-noise ratios. We attribute this behavior to the stronger localization of the near field for sharper tip apexes and thus to a reduction of the sample volume participating in the near-field interaction with the tip, which is not compensated by the increased field enhancement at sharper tip apexes.

In Figure 4, we show results of a numerical study to corroborate and understand the asymmetry of the s-SNOM line profiles observed in our experimental study (Figures 2 and 3). We performed numerical full-wave simulations of the s-SNOM imaging process using the commercial software package Comsol. A conical tip of 8 μm length and apex radius r = 23 nm is placed above a sample modeled by a metal of permittivity $\varepsilon_M = -1200 + 750i$ on the left side (x < 0 nm) and a dielectric material of $\varepsilon_D = 1.05 + 0.19i$ (Al_2O_3)[36] on the right side (x > 0 nm) of the material boundary at x = 0 nm (see illustration in Figure 4a). We assume a p-polarized plane wave illumination (electric field E_{in}) at 32 THz at an angle of α = 60° relative to the tip axis, as in our s-SNOM experiment. The tip-scattered electric field E_{sca} is proportional to the complex-valued dipole moment P, calculated numerically according to[37]

$$E_{sca} \propto P = \int \sigma(\mathbf{r})\mathbf{r}d\mathbf{r}$$

where $\sigma(\mathbf{r})$ is the surface charge density, $\mathbf{r}$ is the radius vector, and the integral is carried out over the whole tip surface. Note that P can be considered as the sum of the tip's dipole moment p_0 arising from the polarization induced by the incoming radiation E_{in} and the induced dipole moment p_{ind} originating from the tip's near-field interaction with the sample, the latter yielding the s-SNOM signal. To simulate the measured s-SNOM signal we have to take into account that the tip is oscillating at frequency Ω, and that the detector signal is demodulated at higher harmonics of Ω. Accordingly, we calculate the scattered field, $E_{sca}(z_t)$, as a function of tip height z_t above the sample. Assuming a vertical sinusoidal motion of the tip with frequency Ω and tapping amplitude A = 24.5 nm, we calculate the time evolution of the detector signal $E_{sca}(z_t(t))$ with $z_t(t)$ = 0.5 nm+ A (1 + cos(Ωt)). The n-th Fourier coefficient of $E_{sca}(z_t(t))$ is then the mathematical analogue of the complex-valued s-SNOM signal $s_n e^{i\phi_n}$. By calculating s_n as a function of tip position x_t, we obtain the simulated line profile $s_n(x_t)$ across the material boundary. The black curve in Figure 4b shows the result obtained for demodulation at n = 4. For comparison, we also show the

DOI: 10.1021/acsphotonics.8b00636
ACS Photonics 2018, 5, 3372−3378

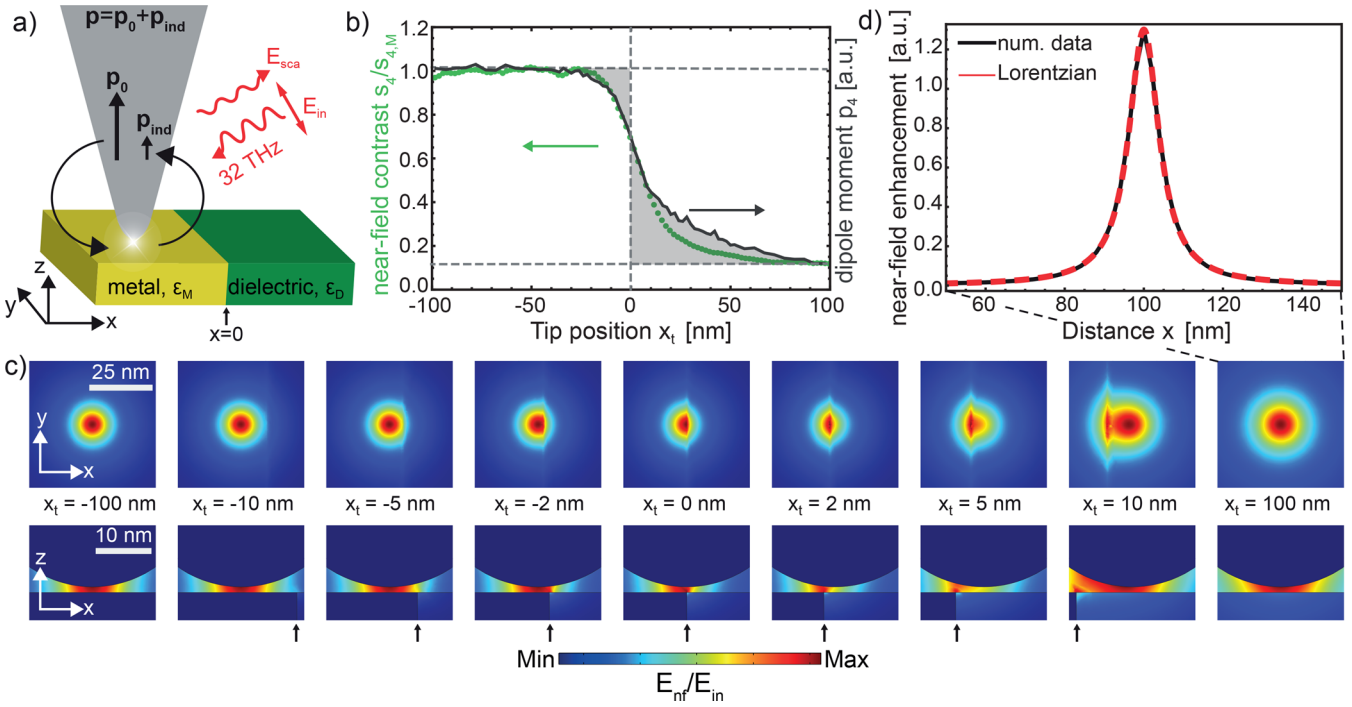

Figure 4. Numerical simulation of IR s-SNOM line profiles. (a) Sketch of the geometry. A tip with apex radius r = 23 nm and length 8 μm is placed above a sample consisting of metal on the left (x < 0 nm) and dielectric material on the right (x > 0 nm) side. The material boundary is at x = 0. (b) Simulated (black curve) and measured (green dots, same data as in Figure 2c) s-SNOM amplitude signal contrast $s_4(x_t)/s_{4,M}(x_t)$ for a tapping amplitude A = 25 nm for different tip positions x_t relative to the material boundary. (c) Electric near-field distribution below the tip apex for different tip positions x_t in the xy-plane (z = 0 nm) and xz-plane (y = 0 nm) for tip−sample separation of 1 nm. The arrow marks the material boundary. (d) Profile of the simulated electric near-field distribution along the x-axis when the tip is placed above the dielectric material (black curve; x_t = 100 nm). Fit of a Lorentzian function (red curve) to the simulated near-field profile.

experimental line profile $s_4(x)$ (green dots, same data as in Figure 2c). A good match between the simulated and the experimental line profiles is found after normalization of both near-field profiles to their average value on the metal. We note that the model overpredicts the asymmetry slightly, essentially on the dielectric side of the material boundary. We explain this observation by differences in tip and sample geometry in experiment and simulations. For example, we simulate a perfect material boundary and a perfect conical metal tip, while in the experiment the sample's material boundary is slightly rounded (see Figure 1) and the tip has a more complicated (pyramidal) shape. We did not take into account the more complicated geometry in the simulation due to limited computation power. We further note that no lateral shift in x-direction was applied to the simulated data (Figure 2c) in order to match the experimental data, which confirms the position of the material boundary found by the fitting procedure introduced in Figure 2. Most importantly, the simulation clearly confirms the asymmetry of s-SNOM line profiles across a material boundary.

To explain the asymmetry of the line profiles, we show in Figure 4d the calculated electric near-field distribution around the tip apex, E_{nf}/E_{in}, for different tip positions x_t. On the metal and dielectric surface, far away from the material boundary at x_t = −100 nm and x_t = 100 nm, respectively, we observe that the near-field distribution in the plane of the sample (xy-plane) is symmetric. However, the near-field confinement is markedly different, indicating a larger probing range of the tip on the dielectric side. When the tip approaches the boundary from the dielectric side, the near-field distribution is already significantly modified at x_t = 10 nm, revealing a near-field interaction with metal across the material boundary. Subsequently, the tip-scattered field and the s-SNOM amplitude signals s_n increase. On the other hand, when the tip approaches the boundary from the metal side, a significant modification of the near-field distribution requires the tip to be closer than 5 nm to the interface (x_t > −5 nm). We explain this finding by the screening of the tip's near fields by the metal sample, which reduces the probing range and prevents the detection of the material boundary via the tip-scattered field for tip-boundary distances larger than 5 nm. The absence of strong near-field screening on the dielectric side thus explains the asymmetry of the s-SNOM line profiles across the boundary between metal and dielectric. In the experiment, the near-field screening by the metal is reduced due to the rounded edge of the material interface (see Figure 1), resulting in a reduced asymmetry of the measured line profiles compared to the simulated one (Figure 4b). We expect that the near-field screening is less important for boundaries between two materials with low dielectric contrast, which would make s-SNOM line profiles more symmetric. We finally note that the electric near-field distribution below the tip apex can be well approximated by a Lorentzian function (Figure 4d). This observation might explain why the s-SNOM line profiles can be well fitted by the integral of Lorentzian functions, but certainly further studies are required for a more comprehensive understanding. Although the presented results are discussed in the context of s-SNOM, we expect the same effect of screening to occur in images acquired by other AFM-based optical microscopy techniques, such as tip-enhanced photothermal expansion microscopy[38] and photoinduced force microscopy[39] that rely on the material profiling via tip-enhanced near fields.

DOI: 10.1021/acsphotonics.8b00636
ACS Photonics 2018, 5, 3372−3378

In summary, we showed that the read/write head of a HDD can serve well as a topography-free test sample for fundamental s-SNOM experiments. It allowed for detailed studies of contrast, resolution, and shape of material boundaries, yielding unprecedented insights into the image contrast formation. Using tips with a standard apex diameter of about 46 nm, we find that the width w of a material boundary in s-SNOM images is around 20 nm, which is in agreement with former reports. However, the line profiles exhibit an asymmetry that has not been observed before, which we corroborate via numerical calculations. The asymmetry can be explained by the tip−sample near-field interaction, which has significant spatial variations across material boundaries. Particularly, we find that the near field at the tip apex is strongly screened on the metal side, which reduces the apparent width of the material boundary in s-SNOM images. We expect that a similar effect will occur at the boundary between two dielectric materials of high and low refractive index because the screening by polarization charges in high-index dielectrics is nearly as large as in metals. Considering this effect will be of critical importance for avoiding misinterpretation of asymmetric line profiles as, for example, continuous (i.e., not sharp) changes of dielectric properties caused by nonuniform doping, directional diffusion, and so on. In the future, it will also be interesting to study how near-field screening affects the spatial resolution when two closely spaced objects are imaged. We further envision that near-field screening could be exploited to increase the s-SNOM resolution for molecule imaging, for example by depositing them on top of a sharp material boundary. We finally note that with custom-made ultrasharp tips of 6 nm diameter we can reduce the apparent material boundary to about 5 nm. On the other hand, both the signal and S/N ratio decrease for sharper tips, which will require to increase the field enhancement at the apex of ultrasharp tips, for example, by engineering and optimizing the antenna performance of the tip shaft.

METHODS

Averaging of Line Profiles. The presented IR and THz line profiles in Figure 2 recorded with the Pt/Ir are the averages of 20 single line profiles. Before averaging, we cross-correlated the line profiles for the second demodulation order $n = 2$ in order to obtain the lateral offset between them. We then corrected for this lateral offset for each demodulation order $n = 2$ to 4. We used the second demodulation order for finding the offsets because it provides a better S/N than higher orders, which enables a higher accuracy of the cross-correlation. For the W-tip line profiles presented in Figure 3, the same procedure was applied using 50 line profiles in total.

FIB Fabrication of Ultra-sharp Tips. The tungsten tips were fabricated by focused ion beam (FIB) machining using a Helios 450s electron microscope (FEI, Netherlands). We used standard Si atomic force microscopy (AFM) cantilevers and first made a cylindrical grove into the tip. Then, a high aspect ratio cone was milled out of a solid tungsten wire, cut at around 12 μm length, and fitted into the cylindrical grove in the Si cantilever. The cone was attached by FIB induced deposition of silicon oxide. Details of this procedure can be found in reference 25. Finally, the tip apex was sharpened by circular ion milling along the tip axis, as described in detail in reference 32. To reach a very small tip apex diameter of 6 nm it is crucial to gradually reduce the milling current down to about 7 pA. Note that fabrication of ultra-sharp tips with radii as small as 3 nm required a hard material such as W. With Pt/Ir we achieved apex radii of about 10 nm and with Au not better than 12 nm. We assign this finding to diffusion of metal atoms under ion bombardment, which is higher for Au than for Pt/Ir and W. Further studies are needed to clarify the mechanisms involved in the tip sharpening process.

ASSOCIATED CONTENT

Supporting Information

The Supporting Information is available free of charge on the ACS Publications website at DOI: 10.1021/acsphotonics.8b00636.

S1: Individual (not-averaged) s-SNOM line profiles recorded with Pt/Ir and W-tips. S2: Comparison of asymmetric vs symmetric fit to s-SNOM line profiles measured with Pt/Ir-tips. S3: Comparison of asymmetric vs symmetric fit to s-SNOM line profiles measured with the W-tip. S4: IR and THz line profiles without vertical offset for comparison of contrast for different demodulation orders (PDF).

AUTHOR INFORMATION

Corresponding Author

*E-mail: r.hillenbrand@nanogune.eu.

ORCID

Stefan Mastel: 0000-0001-9950-5233

Rainer Hillenbrand: 0000-0002-1904-4551

Author Contributions

S.M. and R.H. conceived the study. S.M. fabricated the tips, performed the s-SNOM experiments, fitted the experimental data, and performed the numerical simulations. A.A.G. participated in the fitting and the simulation. C.M. participated in the THz s-SNOM experiments. A.C. proposed the concept and developed the method of FIB fabrication of ultrashap metal tips and recorded the STEM image. A.B. helped with identifying and analyzing the topography-free test sample. All authors discussed the results. R.H. supervised the work. S.M., A.A.G., and R.H. wrote the manuscript with input from all other coauthors.

Notes

The authors declare the following competing financial interest(s): R.H. is co-founder and on the scientific advisory board of Neaspec GmbH, a company producing scattering-type near-field scanning optical microscope systems, such as the one used in this study. The remaining authors declare no competing financial interests.

ACKNOWLEDGMENTS

The authors would like to thank Christopher Tollan (CIC Nanogune, San Sebastián, Spain) for the preparation of a lamella cross section of the sample used in this work, as well as Ken Wood and QMC Instruments Ltd. (Cardiff, U.K.) for providing the bolometer for THz detection. The authors acknowledge financial support from the Spanish Ministry of Economy, Industry, and Competitiveness (National Project MAT2015-65525 and the Project MDM-2016-0618 of the Marie de Maeztu Units of Excellence Program), the H2020 FET OPEN project PETER (GA#767227), and the Swiss National Science Foundation (Grant No. 172218).

DOI: 10.1021/acsphotonics.8b00636
ACS Photonics 2018, 5, 3372−3378

REFERENCES

(1) Keilmann, F.; Hillenbrand, R. In *Nano-Optics and Near-Field Optical Microscopy*; Zayats, A. V., Richards, D., Eds.; Artech House: Boston/London, 2009.
(2) Atkin, J. M.; Berweger, S.; Jones, A. C.; Raschke, M. B. Nano-optical imaging and spectroscopy of order, phases, and domains in complex solids. *Adv. Phys.* **2012**, *61* (6), 745−842.
(3) Muller, E. A.; Pollard, B.; Raschke, M. B. Infrared Chemical Nano-Imaging: Accessing Structure, Coupling, and Dynamics on Molecular Length Scales. *J. Phys. Chem. Lett.* **2015**, *6*, 1275−1284.
(4) Amarie, S.; Zaslansky, P.; Kajihara, Y.; Griesshaber, E.; Schmahl, W. W.; Keilmann, F. Nano-FTIR chemical mapping of minerals in biological materials. *Beilstein J. Nanotechnol.* **2012**, *3*, 312−323.
(5) Amenabar, I.; Poly, S.; Nuansing, W.; Hubrich, E. H.; Govyadinov, A. A.; Huth, F.; Krutokhvostov, R.; Zhang, L.; Knez, M.; Heberle, J.; Bittner, A. M.; Hillenbrand, R. Structural analysis and mapping of individual protein complexes by infrared nanospectroscopy. *Nat. Commun.* **2013**, *4* (2890), na.
(6) Greffet, J.-J.; Carminati, R. Image Formation in Near-field Optics. *Prog. Surf. Sci.* **1997**, *56* (3), 133−237.
(7) Raschke, M. B.; Lienau, C. Apertureless near-field optical microscopy: Tip-sample coupling in elastic light scattering. *Appl. Phys. Lett.* **2003**, *83* (24), 5089−5091.
(8) Lin, K.-T.; Komiyama, S.; Kajihara, Y. Tip size dependence of passive near-field microscopy. *Opt. Lett.* **2016**, *41* (3), 484−487.
(9) Boreman, G. D. *Modulation Transfer Function in Optical and Electro-Optical Systems*; SPIE - The International Society for Optical Engineering: Bellingham, WA, 2001.
(10) Williams, C. S.; Becklund, O. A. *Introduction to the Optical Transfer Function*; SPIE - The International Society for Optical Engineering: Bellingham, WA, 2002.
(11) Smith, W. J. *Modern Optical Engineering*; McGraw Hill: New York City, NY, 2000.
(12) Born, M.; Wolf, E. *Principles of Optics*; Cambridge University Press: Cambridge, 1999.
(13) Hillenbrand, R.; Keilmann, F. Material-specific mapping of metal/semiconductor/dielectric nanosystems at 10 nm resolution by backscattering near-field optical microscopy. *Appl. Phys. Lett.* **2002**, *80* (1), 25−27.
(14) Raschke, M. B.; Molina, L.; Elsaesser, T.; Kim, D. H.; Knoll, W.; Hinrichs, K. Apertureless Near-Field Vibrational Imaging of Block-Copolymer Nanostructures with Ultrathin Spatial Resolution. *ChemPhysChem* **2005**, *6* (10), 2197−2203.
(15) Huber, A. J.; Keilmann, F.; Wittborn, J.; Aizpurua, J.; Hillenbrand, R. Terahertz Near-Field Nanoscopy of Mobile Carriers in Single Semiconductor Nanodevices. *Nano Lett.* **2008**, *8* (11), 3766−3770.
(16) Moon, K.; Do, Y.; Lim, M.; Lee, G.; Kang, H.; Park, K.-S.; Han, H. Quantitative coherent scattering spectra in apertureless terahertz pulse near-field microscopes. *Appl. Phys. Lett.* **2012**, *101* (1), 011109.
(17) Dean, P.; Mitrofanov, O.; Keeley, J. K. I.; Li, L.; Linfield, E. H.; Davies, A. G. Apertureless near-field terahertz imaging using the self-mixing effect in a quantum cascade laser. *Appl. Phys. Lett.* **2016**, *108* (9), 091113.
(18) Moon, K.; Park, H.; Kim, J.; Do, Y.; Lee, S.; Lee, G.; Kang, H.; Han, H. Subsurface Nanoimaging by Broadband Terahertz Pulse Near-field Microscopy. *Nano Lett.* **2014**, *15*, 549−552.
(19) Hecht, B.; Bielefeldt, H.; Inouye, Y.; Pohl, D. W.; Novotny, L. Facts and artifacts in near-field optical microscopy. *J. Appl. Phys.* **1997**, *81*, 2492.
(20) Kalkbrenner, T.; Graf, M.; Durkan, C.; Mlynek, J.; Sandoghdar, V. High-contrast topography-free sample for near-field optical microscopy. *Appl. Phys. Lett.* **2000**, *76* (9), 1206.
(21) Taubner, T.; Hillenbrand, R.; Keilmann, F. Performance of visible and mid-infrared scattering-type near-field optical microscopes. *J. Microsc.* **2003**, *210* (3), 311−314.
(22) Babicheva, V. E.; Gamage, S.; Stockman, M. I.; Abate, Y. Near-field edge fringes at sharp material boundaries. *Opt. Express* **2017**, *25* (20), 23935−23944.
(23) Schnell, M.; Carney, P. S.; Hillenbrand, R. Synthetic optical holography for rapid nanoimaging. *Nat. Commun.* **2014**, *5* (1), 4499.
(24) *Personal Communication*.
(25) Mastel, S.; Lundeberg, M. B.; Alonso-González, P.; Yuando, G.; Watanabe, K.; Taniguchi, T.; Hone, J.; Koppens, F. H. L.; Nikitin, A. Y.; Hillenbrand, R. Terahertz Nanofocusing with Cantilevered Terahertz-Resonant Antenna Tips. *Nano Lett.* **2017**, *17* (11), 6526−6533.
(26) Liewald, C.; Mastel, S.; Hesler, J. L.; Huber, A. J.; Hillenbrand, R.; Keilmann, F. All-electronic terahertz nanoscopy. *Optica* **2018**, *5* (2), 159−163.
(27) Walford, J. N.; Porto, J. A.; Carminati, R.; Greffet, J.-J.; Adam, P. M.; Hudlet, S.; Bijeon, J.-L.; Stashkevich, A.; Royer, P. Influence of tip modulation on image formation in scanning near-field optical microscopy. *J. Appl. Phys.* **2001**, *89* (9), 5159−5169.
(28) Krutokhvostov, R.; Govyadinov, A. A.; Stiegler, J. M.; Huth, F.; Chuvilin, A.; Carney, P. S.; Hillenbrand, R. Enhanced resolution in subsurface near-field optical microscopy. *Opt. Express* **2012**, *20* (1), 593−600.
(29) Govyadinov, A. A.; Mastel, S.; Golmar, F.; Chuvilin, A.; Carney, P. S.; Hillenbrand, R. Recovery of Permittivity and Depth from Near-Field Data as a Step toward Infrared Nanotomography. *ACS Nano* **2014**, *8* (7), 6911−6921.
(30) Knoll, B.; Keilmann, F. Enhanced dielectric contrast in scattering-type scanning near-field optical microscopy. *Opt. Commun.* **2000**, *182*, 321−328.
(31) Bijeon, J.-L.; Adam, P.-M.; Barchiesi, D.; Royer, P. Definition of a simple resolution criterion in an Apertureless Scanning Near-Field Optical Microscope (A-SNOM): contribution of the tip vibration and lock-in detection. *Eur. Phys. J.: Appl. Phys.* **2004**, *26* (1), 45−52.
(32) Huth, F.; Chuvilin, A.; Schnell, M.; Amenabar, I.; Krutokhovstov, R.; Lopatin, S.; Hillenbrand, R. Resonant Antenna Probes for Tip-Enhanced Infrared Near-Field Microscopy. *Nano Lett.* **2013**, *13*, 1065−1072.
(33) Wang, A.; Butte, M. J. Customized atomic force microscopy probe by focused-ion-beam-assisted tip transfer. *Appl. Phys. Lett.* **2014**, *105*, 053101.
(34) Esteban, R.; Vogelgesang, R.; Kern, K. Full simulations of the apertureless scanning near field optical microscopy signal: achievable resolution and contrast. *Opt. Express* **2009**, *17* (4), 2518−2529.
(35) Taubner, T.; Keilmann, F.; Hillenbrand, R. Nanoscale-resolved subsurface imaging by scattering-type near-field optical microscopy. *Opt. Express* **2005**, *13* (22), 8893−8899.
(36) Palik, E. D. *Handbook of Optical Constants of Solids II*; Academic Press: London, 1991.
(37) Jackson, J. D. *Classical Electrodynamic*; John Wiley and Sons, Inc: Hoboken, NJ, 1999.
(38) Lu, F.; Mingzhou, J.; Belkin, M. A. Tip-enhanced infrared nanospectroscopy via molecular expansion force detection. *Nat. Photonics* **2014**, *8* (4), 307−312.
(39) Rajapaksa, I.; Uenal, K.; Wickramasinghe, H. K. Image force microscopy of molecular resonance: A microscope principle. *Appl. Phys. Lett.* **2010**, *97* (7), 073121.

DOI: 10.1021/acsphotonics.8b00636
ACS Photonics 2018, 5, 3372−3378